Calibration of the UV/Ion Shields for the AXAF High Resolution Camera

G.R. Meehan, S.S. Murray, M.V. Zombeck, R.P. Kraft, K. Kobayashi,
J.H. Chappell, A.T. Kenter
Smithsonian Astrophysical Observatory, 60 Garden St., Cambridge, MA 02138

and

M. Barbera, A. Collura, S. Serio
Istituto e Osservatorio Astronomico G.S. Vaiana, Palermo, Italy, 90123

ABSTRACT

The High Resolution Camera (HRC) is one of AXAF's two focal plane instruments. It consists of two detectors: the HRC-I which is optimized for direct imaging of x-ray sources; and the HRC-S which is optimized as the spectroscopic read-out of the Low Energy Transmission Grating (LETG). Both detectors are comprised of a chevron pair of micro-channel plates (MCPs) with a crossed grid charge detector (CGCD) and a UV/Ion shield (UVIS). The role of the UVIS is to minimize the detectors' sensitivity to low energy electrons, ions and UV light, while providing sufficient x-ray transmission in the 0.1 to 10 keV x-ray band. In this paper, we report on the results of the flight UVIS calibration measurements. Specifically, x-ray and UV transmission measurements obtained at the HRC X-ray Test Facility of the Smithsonian Astrophysical Observatory, and x-ray transmission measurements of UVIS witness samples obtained at a synchrotron light source facility.

Keywords: X-ray detectors, UV/Ion Shield, AXAF, High Resolution Camera.

1 Introduction

The Advanced X-ray Astrophysics Facility (AXAF)[1,2] is scheduled for launch in late 1998. One of its two focal plane instruments is the High Resolution Camera (HRC).[3,4]

The HRC consists of two detectors; an imaging detector with an approximate 0.5 arcsec FWHM resolution (HRC-I), and a spectroscopic read-out detector for the Low Energy Transmission Grating (LETG)[5,6,7] that has an approximate 0.05 Å resolution (HRC-S). The HRC-I is comprised of two 10 cm × 10 cm microchannel plates (MCPs) assembled into the chevron configuration. The MCPs were manufactured by the Galileo Electro-Optics Corporation (GEOC). A CsI photocathode is deposited on the top, or input, MCP to enhance its quantum efficiency (QE). The HRC-S (whose MCPs were manufactured by Philips Photonics) is comprised of 3 segments, each of which is a chevron pair of 30 mm × 100 mm MCPs. To enhance its QE, the top MCP of each segment is also coated with CsI. Both detectors employ low-noise (i.e., reduced radioisotope content) glass, yielding an internal background of ≤ 0.03 counts s^{-1} cm^{-2} over the entire detector. A UV/ion shield (UVIS) is incorporated onto the front of each detector assembly to prevent diffuse UV radiation and charged particles (i.e., low energy ions and electrons) from becoming the dominant source of detector background. Consequently, the UVIS plays a crucial role in the successful operation of the HRC. Calibration of the UV/ion shields is necessary to fully quantify the HRC-I and HRC-S response to x-rays and the UV.

In this paper, we report on the results of x-ray, synchrotron, and UV transmission measurements performed on UVIS witness samples.

2 SAO X-ray Monochromator Transmission Measurements

Every UV/ion shield supplied to us by the Luxel Corporation (Friday Harbor, WA) was accompanied by two witness samples, each of which is 16mm in diameter. Each pair of witness samples comes from the same filter production run as its associated flight filter, and are taken from different regions of the larger filter sheet. The experimental setup precluded any effort to perform spatial uniformity measurements on a given witness sample. Rather, each measurement represents an average transmission over a filter. However, we know from previous uniformity measurements of a candidate HRC-I UV/ion shield, that it was spatially uniform in transmission within 5% relative error at a spatial scale of 1 mm.[8] All of the flight witness samples, and several non-flight witness samples, tested within this work are listed in table 1. Included in this table are the thickness values of the constituent layers as reported by Luxel. Figure 1 shows the nominal thickness values of the HRC-I and HRC-S UV/ion shields.

2.1 Instrumental Setup

The transmission measurements were carried out at the SAO using a McPherson model 248/310 G 1-meter diameter grazing incidence monochromator. It is equipped with a 600 G/mm grating that has a 1^o blaze angle and a $580\AA$ blaze wavelength, which yields an operating range of 6 $\AA$ to 681 $\AA$ and a resolution of 0.5 $\AA$. The monochromator entrance and exit slits were set to a nominal 15 μm width to minimize contamination by the x-ray continuum. Figure 2 represents a typical monochromator beam scan to identify the fluorescent lines associated with the anode selected for use in the Manson model 2 single-anode soft x-ray source. In this case, titanium. The scan shows that the Ti L_α and L_η lines dominate over the continuum by about a factor of 10. The O K_α line is even more dominant. When a line is selected, the monochromator is adjusted to operate at the line peak. The instrument is also equipped with a pair of filter wheels, each of which has enough holders to accomodate up to five witness samples. However, one holder of each wheel was intentionally left unoccupied so that x-ray spectra could be obtained without a filter in the x-ray detector beam path as part of the transmission measurement procedure. Spectra were acquired with a Manson model 851 gas-flow proportional counter equipped with a VYNS window, and which utilized methane as the fill gas.

2.2 Results

The procedure for making a transmission measurement involved obtaining a pair of filter-in/filter-out spectra, as well as a background spectrum. Once the background contribution was subtracted from both x-ray spectra, the value of the transmission simply involved dividing the number of remaining counts in the filter-in measurement by the number of remaining counts in the filter-out measurement. The measurement results are shown as the data points in figures 3 through 7.

2.3 Modelling the X-ray Transmission

A model of x-ray transmission for each witness sample was obtained by applying a nonlinear fitting routine (the Levenberg-Marquardt algorithm) to each data set. The transmission of x-rays through N layers of material is represented by

$$T(E) = \prod_{i=1}^{N} e^{-(\frac{\mu(E)}{\rho})_i(\rho t)_i} \tag{1}$$

where the product of the material density and thickness, ρ and t, respectively, is called the mass areal density. In fitting a model to the data, the mass areal densities of Al, C, N and O were adjusted in such a way as to minimize the reduced χ^2 value of the fit. The mass absorption coefficient of a particular element, $(\frac{\mu}{\rho})$, is related to the imaginary part of the atomic scattering factor, f_2, by the expression

$$\frac{\mu(E)}{\rho} = 2r_e hcN_o \frac{f_2}{AE} \tag{2}$$

where r_e is the classical electron radius, h is Plank's constant, c is the speed of light, N_o is Avagadro's number, and A is the atomic mass of the element.

The mass absorption coefficients are taken from Henke, *et al*, (1982)[9], as opposed to the 1993 values[10]. We believe that the 1993 Henke values for carbon and aluminum are suspect. We have come to this conclusion for the following three reasons. First, from the results of an unrelated experiment to measure the counter depth of our gas-flow proportional counters, we were able to conclude that the 1982 values for carbon yielded counter depths consistent with the manufacturer's specifications. However, computations using the 1993 values resulted in counter depths that were 20% larger, exceeding the physical size of the detectors themselves. Indeed, Gullikson concurs with these particular findings pertaining to the carbon data.[11] As a second example, the 1993 values consistently yield reduced χ^2 values for our transmission models that are greater than what are obtained when the 1982 values are used. And third, the resultant aluminum thickness of all witness samples agreed well with Luxel's values for only the 1982 coefficients. This is brought out clearly in table 2, where Luxel's measurement of aluminum thickness for each witness sample is compared with the thickness values that we derived from using the 1982 and 1993 Henke coefficients. Note that the canonical density of aluminum, when deposited in a thin layer, is 2.50 g-cm^{-3}. In each case, only the 1982 coefficients yield values of aluminum thickness that agree with Luxel's, within the limits of error.

The areal densities of Al, C, N and O for each witness sample are listed in table 3. The reduced χ^2 for both the 1982 and 1993 Henke coefficients are included. The modelled transmission curve for each witness sample, along with the associated data set, is shown in figures 3 through 7. A plot of the relative residuals, $(\frac{data-fit}{data})$ for one transmission curve is shown in figure 8. The dashed horizontal line in the plot represents the median of the relative residuals. The fact that the median is close to zero for the filter shows that systematic errors are negligible. The other transmission curves are similar.

By adding up the areal densities of C, N and O for any given witness sample, one obtains the areal density of polyimide. Dividing by the canonical density of polyimide, 1.40 gm-cm^{-3}, yields the thickness of the material. The areal density (and hence thickness) of polyimide is under estimated, as the hydrogen areal density is not included in the thickness derivation. However, its contribution is negligible compared to the other three elements. The derived polyimide thicknesses of the samples are shown in table 4.

3 Synchrotron X-ray Transmission Measurements

In order to define an accurate model of X-ray Absorption Near Edge Structures (XANES), high spectral resolution x-ray transmission measurements in the energy range of 70-1950 eV were conducted on four witness samples at the BESSY 1 synchrotron in Berlin, Germany.

3.1 Instrumental Setup

The measurements were conducted at station 11.31 of the Physikalisch-Technische Bundesanstalt (PTB) radiometry laboratory[12,13] at the BESSY 1 synchrotron. The beam-line includes an SX-700 type plane grating monochromator[14] with a useful photon energy range of 60 - 2000 eV and spectral resolution ranging from $E/\Delta E = 2500$ at 100 eV to $E/\Delta E = 700$ at the Al-K edge. A test chamber (700 mm long, 600 mm in diameter) was provided with a vacuum-compatible micro-positioning system for the manipulation of witness samples and detectors. Two detectors were used: a GaP/Au Schottky-type photodiode (Hamamatsu G1963) with a sensitive area of 4.6 mm×4.6 mm; and a VALVO X913 BL channel electron multiplier (CEM). The photodiode performs well and is actually used at all surveyed energies with the exception of the 283-300 eV range, where the CEM is more appropriate because of the low flux available in that region.

The four samples that were studied are listed in table 1. They were mounted on a four-position fixture (one position left open) attached to a micro-positioning system allowing complete two dimensional scans of the samples. A 400 μm spot size was chosen as the best compromise between flux stability and spatial resolution. Table 5 describes the energy scans in detail.

Each individual measurement at a given energy is the average of 3 independent consecutive detector readings. If the readings are not consistent with each other to within 1%, the measurement is automatically repeated. Each measurement is normalized by the current of the beam in the storage ring. This procedure accounts for the time dependence of the beam, ensuring measurement stability at the 1% level over a time scale of 30 minutes. In order to ensure no significant drift between measurements at the open and sample positions, all of our measurement sets were taken over time scales shorter than 10 minutes.

The measurement technique described above ensures a statistical uncertainty within 1% at all energies. Stray light contribution in the monochromatic radiation between 1.0 and 1.7 keV is up to 2%, resulting in a transmission uncertainty within 1% for measured samples like ours. Above 1.7 keV, the stray light contamination is higher, and results in a measurement uncertainty up to 3%. Second order contamination is particularly significant at low energies ($E < 130$ eV), and in a small region above the carbon edge (290-300 eV), resulting in a measurement uncertainty of up to 30%. Outside of these regions, the measurement uncertainties are always lower than 3%.

3.2 Results

Previous synchrotron measurements conducted on witness samples of candidate HRC UV/Ion shields[15] revealed no significant spatial variation of the near edge absorption structures. We therefore tested only one witness sample for spatial variations of the fine structures. Figure 9 shows in detail the transmission measurements near the absorption K-edges of C, N, O, and Al for the two locations surveyed on the witness sample TF101-1174. These measurements again confirm that no significant spatial variations (at 0.4 mm resolution) are observed for the absorption fine structures. We expect a similar variation in transmission at this spatial scale for the flight HRC-I UV/ion shield, as it is derived from the same multi-layer sheet of film as this witness sample.

The measured transmission for the four tested samples are reported in figures 10 through 13. In these plots, the transmission data (along with the associated error bars) are superimposed over the best-fit curve. The data, with the exception of small energy regions around the absorption edges, have been fitted with the x-ray transmission model described in section 2.3. Table 6 reports the best fit parameters for the mass areal density of C, N, O, and Al. For comparison, those witness samples with matching run numbers that were measured with the SAO x-ray monochromator are included. Notice that the best fit parameters derived from the two test methods for the two witness samples associated with run number 6550-8 (which have the same material thicknesses) agree within the error limits. A similar statement can be made for the witness samples associated with run number 6788-8. The pair of witness samples associated with run number 6569-8 (TF100-354 and TF101-1092), and the pair of witness samples associated with run number 6567-8 (TF101-891 and TF100-565), each represents different regions of an HRC-S outer segment flight UV/ion shield. For a given pair of witness samples, the best fit parameters for C, N and O are comparable, within the uncertainties. This is consistent with the fact that the polyimide thickness of the filter pair is the same. Since a given pair of witness samples represents different regions of a flight HRC-S filter, the aluminum thicknesses are not equal. This is reflected by the difference in their respective mass areal densities. Table 7 shows that, for each such pair of witness samples, the ratio of the mass areal densities of aluminum agrees with the ratio of the thickness values measured by Luxel, within the uncertainties. Table 4 lists the derived polyimide thicknesses for the samples tested with the synchrotron source, while table 8 lists their derived aluminum thicknesses. For comparison, Luxel's thickness measurements are included in both tables.

The mass attenuation coefficient derived for a compound by taking into account only the individual atomic coefficients does not take into consideration fine structure features that occur near the absorption edges due to interactions of the photoelectrons with the closer atoms in the molecules of the compound (XANES and EXAFS). In order to define the mass attenuation coefficients of a compound that include these features, direct transmission measurements need to be conducted on the compound material of interest. Following the same technique described by us in an earlier work[15], we have used the synchrotron measurements and the above mentioned best fit model parameters of witness sample TF101-1174 (the sample with the thickest layer of polyimide) to derive the mass attenuation coefficients of C, N, and O near their K absorption edges. Analogously, we have used the measurements and the best fit model parameters of witness sample TF101-891 (the sample with the thickest layer of aluminum) to derive the mass attenuation coefficients of Al near its K and L absorption edges. Adopting the mass attenuation coefficients now extended to the absorption edge regions, we have built new transmission models for the four samples (refer to figures 10 through 13). The x-ray transmission model, which incorporates the newly derived mass attenuation coefficients near the absorption edges with the literature-based mass attenuation coefficients outside of the absorption edges[9], is in very good agreement with our measurements. Figure 14 gives a detailed view of how well the transmission model agrees with the measurements near the K-edge absorption regions for C, N, O and Al for filter TF100-354, while figure 15 shows the relative residuals between the transmission measurements of this filter and the associated model. Note that these plots show that there is good agreement between the measurements and the fit, except at several energies near the carbon K-edge absorption region. There are two possible explanations for this discrepancy. The first is that we have under-estimated the error in the measured transmission due to higher order contamination (that is, 3^{rd} order and higher) from carbon. The second is that there is a dependence of the transmission on features in the filter itself, though we consider this to be unlikely. We are continuing to investigate this issue. Despite this discrepancy at carbon, we obtain very good agreement between the measurements and the fits near the K-edge absorption regions for N, O and Al for all four filters that were tested. Also, the peaks of the modelled transmission curves occur at the same energy locations for all four filters in each of the four near-edge absorption regions. This model can be extended to filter samples of the same material composition, but of different thicknesses, provided that the mass areal densities of C, N, O, and Al are derived from the best fit analysis on a small number of measurements like those reported on in section 2. The mass absorption coefficients derived near the K-edge absorption regions of C, N, O and Al are depicted in figure 16. Included in each graph is a line plot that represents the 1982 Henke coefficients.

4 UV and Visible Light Measurements

A third aspect to the calibration of the UV/ion shield witness samples is the development of UV light transmission models. This is an on-going task, for which it will be necessary to perform transmission measurements in the visible and near UV. We have, however, started the process of measuring the UV transmission of the witness samples at 1470 Å and at 2537 Å. The results to-date of these particular measurements are the subject of this section.

Due to the extremely low UV transmission of the witness samples, the method of performing a sequence of filter-in/filter-out measurements is impractical. Instead, we measured the flux of photons from a UV light source that passed through the witness sample under test. We also determined the photon flux of the UV light source itself. The ratio of the photon flux transmitted through the witness sample to the photon flux of the UV source yields the transmission at that particular wavelength.

To measure the photon flux transmitted through the witness sample, the test configuration shown in figure 17 is used. The witness sample under test is mounted onto a Schlumberger EMR photomultiplier tube (model 541F-09-17). To measure the UV flux through the witness sample at 1470 Å, we employed an ultraviolet calibration xenon lamp (EMR Photoelectric, model 582X-05). A UV interference filter with a peak transmission of 10% at 1470 Å was mounted in front of it. At 2537 Å, we used a mercury light source (Pen-Ray, model 11 SC-1) in combination with an interference filter that has a peak transmission of about 15% at 2537 Å.

The UV beam flux from each lamp was measured with a NIST UV photodiode (Ball Aerospace, serial no. 94-3). Its 25mm-diameter sensitive area was stopped down to 12.5mm so that the detector would subtend the same solid angle at the source as the PMT photocathode did. The photodiode has a quantum efficiency of 9.1% at 1470 Å, and of 14.3% at 2537 Å.

Table 9 lists the UV transmission measurements that have been obtained as of this writing. In addition, Luxel's visible light transmission measurements are included. In each case, the transmission results meet the scientific requirements. Also, that we obtained such low transmission values indicates that there are no pinholes in any of the witness samples.

5 Conclusion

We have carried out a program of calibrating the flight, and several non-flight, witness samples associated with the HRC-I and HRC-S UV/ion shields. As a result of measuring the transmission of the samples with an x-ray monochromator, we have successfully developed transmission models based on the mass areal densities of Al, C, N and O. This achievement has been the result of basing our models on the 1982, rather than 1993, Henke tables, as we feel that the 1993 values for carbon and aluminum are suspect.

High spectral resolution x-ray transmission measurements were carried out on four flight witness samples at the BESSY1 synchrotron source in Berlin, Germany, to define an accurate model of X-ray Absorption Near Edge Structures. Our results show that no significant spatial variations in transmission at the 0.4 mm resolution are observed for the absorption fine structures. The data, with the exception of small-energy regions around the absorption structures, have been fitted with the same model described for the monochromator results. This model has been extended to take into account the fine structures near the absorption edges, and is in very good agreement with the synchrotron measurements.

Finally, UV transmission measurements carried out on the witness samples at 1470 Å and at 2537 Å has yielded results that satisfy the scientific requirements. The measurements also indicate that all of the witness samples tested to-date are free of any pinhole features.

6 Acknowledgments

We gratefully acknowledge the laboratory support of Frank Rivera at the HRC Laboratory of the SAO.

We would also like to thank Marco Wedowski, Peter Bulicke, and Stefan Kraft of PTB laboratory at BESSY for their assistance in obtaining and analyzing the synchrotron data, and acknowledge partial support from Ministero dell'Università e della Ricerca Scientifica, Agenzia Spaziale Italiana (MB, AC, SS), and CNR (AC).

This work has been supported by NASA contract NAS8-38248.

7 References

1. M.V. Zombeck, "Advanced X-ray Astrophysics Facility (AXAF)," Proceedings of the International School of Space Science, Course on 'X-ray Astronomy', Aquila, Italy, 1996, preprint.
2. M.C. Weisskopf, S.L. O'Dell, R.F. Elsner, and L.P. Van Speybroeck, "Advanced X-ray Astrophysics Facility AXAF - an overview," Proc. SPIE, 2515, 1995
3. S.S. Murray, J.H. Chappell, A.T. Kenter, K. Kobayashi, R.P. Kraft, G.R. Meehan, M.V. Zombeck, "AXAF High Resolution Camera (HRC)", Proc. SPIE, 3114, 1997
4. M.V. Zombeck, J.H. Chappell, A. Kenter, R.W. Moore, S.S. Murray, "The High Resolution Camera (HRC) on the Advanced X-ray Astrophysics Facility (AXAF)," Proc. SPIE, 2518, 1996
5. A.C. Brinkman, J.J. van Rooijen, J.A.M. Bleeker, J.H. Dijkstra, J. Heise, P.A.J. De Korte, R. Mewe and F. Paerels, "Low Energy X-ray Transmission Grating Spectrometer for AXAF," *Astro. Lett. and Communications*, 1987, Vol. 26, pp. 73-86.
6. A.C. Brinkman, C.J. Th. Gunsing, J.S. Kaastra, H. Brauninger, J.J. Drake, J.Z. Juda, M. Juda, D. Dewey, K.A. Flanagan, H.L. Marshall, "Preliminary Test Results on Spectral Resolution of the Low Energy Transmission Grating Spectrometer on Board of AXAF," 1997, SPIE conference - San Diego
7. P. Predehl, H. Brauninger, A.C. Brinkman, D. Dewey, J.J. Drake, K.A. Flanagan, T. Gunsing, G.D. Hartner, J.Z. Juda, M. Juda, J. Kaastra, H.L. Marshall, D. Swartz, "X-Ray Calibration of the AXAF Low Energy Transmission Grating Spectrometer: Effective Area," 1997, SPIE conference - San Diego
8. G.R. Meehan, A.T. Kenter, R.P. Kraft, S.S. Murray, M.V. Zombeck, K. Kobayashi, J.H. Chappell, M. Barbera, and A. Collura, "Measurement of the transmission of the UV/Ion Shields for the AXAF High Resolution Camera," Proc. SPIE, 2808, 1996.
9. B.L. Henke, *et al.*, *Atom. Data and Nucl. Data Tables*, 27, 1982.
10. B.L. Henke, E.M. Gullikson, and J.C. Davis, *Atom. Data and Nucl. Data Tables*, 54(2), 1993.
11. E.M. Gullikson, 1997. Private communications.
12. D. Fuchs, M. Krumrey, P. Muller, F. Scholze, and G. Ulm, "High precision soft x-ray reflectometer," February 1995, Rev. Sci. Instr. 66 (2).
13. G. Ulm, and B. Wende, "Radiometry laboratory of Physikalisch-Technische Bundesanstalt at BESSY," February 1995, Rev. Sci. Instr. 62 (2).
14. F. Scholze, M. Krumrey, P. Muller, and D. Fuchs, "Plane grating monochromator beamline for VUV Radiometry," October 1994, Rev. Sci. Instr., 65 (10).
15. Barbera, M., Collura, A., Dara, A., "Calibration of the AXAF-HRC UV/Ion shields at Osservatorio Astronomico di Palermo G.S. Vaiana: III - Synchrotron measurements of XANES in aluminum coated Lexan film samples," 1996, SPIE vol. 2808, 120.

8 Tables and Figures

Witness Sample	Run Number	Composition and Luxel Thickness Measurements	Status	Test Method
TF100-354	6569-8	Aluminum $305 \pm 30\AA$ Polyimide $1940 \pm 100\AA$	Flight	Synchrotron
TF100-565	6567-8	Aluminum $315 \pm 30\AA$ Polyimide $2040 \pm 100\AA$	Flight	SAO Monochromator
TF101-883	6747-8	Aluminum $790 \pm 50\AA$ Polyimide $5215 \pm 100\AA$	Non-Flight	SAO Monochromator
TF101-891	6567-8	Aluminum $315 \pm 30\AA$ Aluminum $1710 \pm 50\AA$ Polyimide $2040 \pm 100\AA$	Flight	Synchrotron
TF101-914	6492-8	Polyimide $5039 \pm 100\AA$ Aluminum $735 \pm 50\AA$ Carbon $240 \pm 25\AA$	Non-Flight	SAO Monochromator
TF101-1052	6550-8	Aluminum $665 \pm 50\AA$ Polyimide $2500 \pm 100\AA$ Aluminum $307 \pm 30\AA$	Flight	SAO Monochromator
TF101-1053	6550-8	Aluminum $665 \pm 50\AA$ Polyimide $2500 \pm 100\AA$ Aluminum $307 \pm 30\AA$	Flight	Synchrotron
TF101-1054	6547-8	Aluminum $643 \pm 50\AA$ Aluminum $302 \pm 30\AA$ Polyimide $2500 \pm 100\AA$	Non-Flight	SAO Monochromator
TF100-1063	6080-5	Polyimide $2265 \pm 100\AA$	Non-Flight	SAO Monochromator
TF101-1092	6569-8	Aluminum $1663 \pm 50\AA$ Aluminum $305 \pm 30\AA$ Polyimide $1940 \pm 100\AA$	Flight	SAO Monochromator
TF101-1174	6788-8	Aluminum $795 \pm 50\AA$ Polyimide $5300 \pm 100\AA$	Flight	SAO Monochromator Synchrotron
TF101-1175	6788-8	Aluminum $795 \pm 50\AA$ Polyimide $5300 \pm 100\AA$	Flight	SAO Monochromator

Table 1. Description of the witness samples that were tested with the SAO x-ray monochromator, and at the BESSY1 Synchrotron Light Source Facility. The material composition and flight status of each filter is included.

Witness Sample	Run Number	Luxel (Å)	Henke 1982 (Å)	Henke 1993 (Å)
TF100-565	6567-8	315 ± 30	316.8 ± 18.8	277.2 ± 17.2
TF101-883	6747-8	790 ± 50	777.6 ± 19.6	652.4 ± 18.4
TF101-914	6492-8	735 ± 50	693.2 ± 20.0	592.8 ± 18.4
TF101-1052	6550-8	972 ± 58	952.8 ± 18.0	792.8 ± 18.4
TF101-1054	6547-8	945 ± 58	866.0 ± 18.0	714.8 ± 17.2
TF100-1063	6080-5	0	0.0 ± 5.6	4.8 ± 7.2
TF101-1092	6569-8	1968 ± 58	1906.0 ± 26.8	1678.4 ± 26.0
TF101-1174	6788-8	795 ± 50	759.6 ± 20.4	640.6 ± 18.1
TF101-1175	6788-8	795 ± 50	766.0 ± 19.2	642.8 ± 18.8

Table 2. Comparison of aluminum thickness values as measured by Luxel, with the thickness values derived from the SAO x-ray monochromator data fitted using the 1982 and 1993 Henke coefficients. Note that only the 1982 Henke values yield thickness values that agree with Luxel's measurements, within the statistical uncertainties.

Witness Sample	Al (μg/cm^2)	C (μg/cm^2)	N (μg/cm^2)	O (μg/cm^2)	Reduced χ^2 (1982)	Reduced χ^2 (1993)
TF100-565	7.92 ± 0.47	21.10 ± 0.66	1.05 ± 1.00	6.62 ± 1.25	1.139	3.650
TF101-883	19.44 ± 0.49	53.79 ± 1.16	6.33 ± 1.22	16.26 ± 1.35	2.785	17.23
TF101-914	17.33 ± 0.50	58.50 ± 1.20	6.98 ± 1.28	15.43 ± 1.34	6.289	19.453
TF101-1052	23.82 ± 0.45	26.33 ± 0.71	2.34 ± 0.91	9.83 ± 1.19	3.997	26.238
TF101-1054	21.65 ± 0.45	25.73 ± 0.71	2.18 ± 0.90	9.70 ± 1.15	3.404	23.511
TF100-1063	0.00 ± 0.14	24.32 ± 0.54	2.31 ± 0.81	6.11 ± 0.53	2.888	5.313
TF101-1092	47.65 ± 0.67	21.74 ± 0.83	1.79 ± 0.96	6.62 ± 1.38	3.499	16.529
TF101-1174	18.99 ± 0.51	54.01 ± 1.13	6.80 ± 1.21	16.02 ± 1.47	2.448	18.119
TF101-1175	19.15 ± 0.48	55.09 ± 1.13	5.91 ± 1.21	16.76 ± 1.35	1.688	19.856

Table 3. Computed mass areal densities based on 1982 Henke coefficients for witness samples measured with the SAO x-ray monochromator. The reduced χ^2 values of the data fits for both the 1982 and 1993 Henke coefficients are included to show that the 1982 Henke values yield significantly improved fits.

Witness Sample	Run Number	Luxel Thickness ($\AA$)	Derived Thickness ($\AA$)	Test Method
TF100-354	6569-8	1940 ± 100	2120 ± 64	Synchrotron
TF100-565	6567-8	2040 ± 100	2060 ± 124	SAO Monochromator
TF101-883	6747-8	5215 ± 100	5460 ± 154	SAO Monochromator
TF101-891	6567-8	2040 ± 100	2100 ± 91	Synchrotron
TF101-914	6492-8	5039 ± 100	5780 ± 158	SAO Monochromator
TF101-1052	6550-8	2500 ± 100	2750 ± 118	SAO Monochromator
TF101-1053	6550-8	2500 ± 100	2620 ± 79	Synchrotron
TF101-1054	6547-8	2500 ± 100	2670 ± 116	SAO Monochromator
TF100-1063	6080-5	2265 ± 100	2340 ± 79	SAO Monochromator
TF101-1092	6569-8	1940 ± 100	2150 ± 134	SAO Monochromator
TF101-1174	6788-8	5300 ± 100	5490 ± 158	SAO Monochromator
TF101-1174	6788-8	5300 ± 100	5490 ± 119	Synchrotron
TF101-1175	6788-8	5300 ± 100	5550 ± 152	SAO Monochromator

Table 4. The derived polymide thicknesses for the witness samples are compared against Luxel's measured values. Thicknesses are derived from both the SAO monochromator and the synchrotron data. The hydrogen areal density was not incorporated into the derived values, though it makes a negligible contribution to the polyimide areal density.

Beam Filter	Energy range (eV)	energy step (eV)	Absorption Edge
Beryllium 0.25 μm	$60 - 71$	1	
Beryllium 0.25 μm	$71.2 - 75$	0.2	Aluminum LII,LIII
Beryllium 0.25 μm	$76 - 110$	1	
No Filter	$100 - 250$	2	
Titanium 1 μm	$250 - 280$	2	
Titanium 1 μm	$280.5 - 293$	0.5	Carbon K
Titanium 1 μm	$295 - 400$	5	
Titanium 1 μm	$400.2 - 415$	0.2	Nitrogen K
Titanium 1 μm	$416 - 450$	1	
Iron 0.5 μm	$450 - 520$	3	
Iron 0.5 μm	$521 - 529$	1	
Iron 0.5 μm	$529.2 - 540$	0.2	Oxygen K
Iron 0.5 μm	$541 - 565$	1	
Iron 0.5 μm	$541 - 600$	1	
Iron 0.5 μm	$605 - 700$	5	
Copper 0.5 μm	$700 - 900$	5	
Berylium 7 μm	$900 - 1540$	10	
Berylium 7 μm	$1542 - 1600$	2	Aluminum K
Berylium 7 μm	$1605 - 1700$	5	
Berylium 7 μm	$1710 - 1950$	10	

Table 5. Energies surveyed in the synchrotron transmission measurements.

Witness Sample	Run Number	Al (μg/cm^2)	C (μg/cm^2)	N (μg/cm^2)	O (μg/cm^2)	Test Method
TF100-354	6569-8	7.26 ± 0.16	20.94 ± 0.62	1.68 ± 0.52	7.11 ± 0.40	Synchrotron
TF101-1092	6569-8	47.65 ± 0.67	21.74 ± 0.83	1.79 ± 0.96	6.62 ± 1.38	SAO Monochromator
TF101-891	6567-8	50.34 ± 0.45	20.00 ± 0.93	1.84 ± 0.75	7.54 ± 0.45	Synchrotron
TF100-565	6567-8	7.92 ± 0.47	21.10 ± 0.66	1.05 ± 1.00	6.62 ± 1.25	SAO Monochromator
TF101-1053	6550-8	24.54 ± 0.25	25.68 ± 0.78	2.06 ± 0.65	8.88 ± 0.44	Synchrotron
TF101-1052	6550-8	23.82 ± 0.45	26.33 ± 0.71	2.34 ± 0.91	9.83 ± 1.19	SAO Monochromator
TF101-1174	6788-8	19.93 ± 0.18	55.37 ± 1.25	5.75 ± 0.99	15.75 ± 0.49	Synchrotron
TF101-1174	6788-8	18.99 ± 0.51	54.01 ± 1.13	6.80 ± 1.21	16.02 ± 1.47	SAO Monochromator
TF101-1175	6788-8	19.15 ± 0.48	55.09 ± 1.13	5.91 ± 1.21	16.76 ± 1.35	SAO Monochromator

Table 6. The mass areal densities from the best fit results of the x-ray synchrotron transmission measurements, compared to matching witness samples (run numbers) from the SAO monochromator results.

Witness Sample Pairing	Ratio of Al Mass Areal Densities	Ratio of Luxel Al Thickness values
TF101-1092 TF100-354	6.56 ± 0.17	6.45 ± 0.69
TF101-891 TF100-565	6.36 ± 0.38	6.43 ± 0.66

Table 7. A comparison of the ratio of Al mass areal densities of two pairs of witness samples with the ratio of the aluminum thickness values measured by Luxel.

Witness Sample	Run Number	Luxel Al Measured Thickness ($\AA$)	Derived Al Thickness ($\AA$)
TF100-354	6569-8	305 ± 30	290 ± 6.4
TF101-891	6567-8	2025 ± 58	2014 ± 18.0
TF101-1053	6550-8	972 ± 58	981.6 ± 10.0
TF101-1174	6788-8	795 ± 50	797.2 ± 7.2

Table 8. The derived aluminum thicknesses for the witness samples measured with the synchrotron x-ray source are compared to Luxel's measurements. Note that the two sets of values agree, within the statistical uncertainties.

Witness Sample	UV Transmission at 1470 $\AA$	UV Transmission at 2537 $\AA$	Luxel Visible Light Measurement
TF101-883	4.7×10^{-11}	4.4×10^{-12}	4.25×10^{-5}
TF101-1052	7.9×10^{-8}	1.4×10^{-8}	9.57×10^{-6}
TF101-1053	9.3×10^{-8}	7.8×10^{-9}	9.59×10^{-6}
TF101-1054	2.1×10^{-7}	1.1×10^{-8}	3.75×10^{-5}
TF101-1174	4.4×10^{-11}	5.8×10^{-12}	3.73×10^{-5}
TF101-1175	5.0×10^{-11}	4.4×10^{-12}	3.21×10^{-5}

Table 9. The UV transmsission measurement results at 1470 $\AA$ and at 2537 $\AA$ that have been completed to-date are listed above. Luxel's visible light measurements are included.

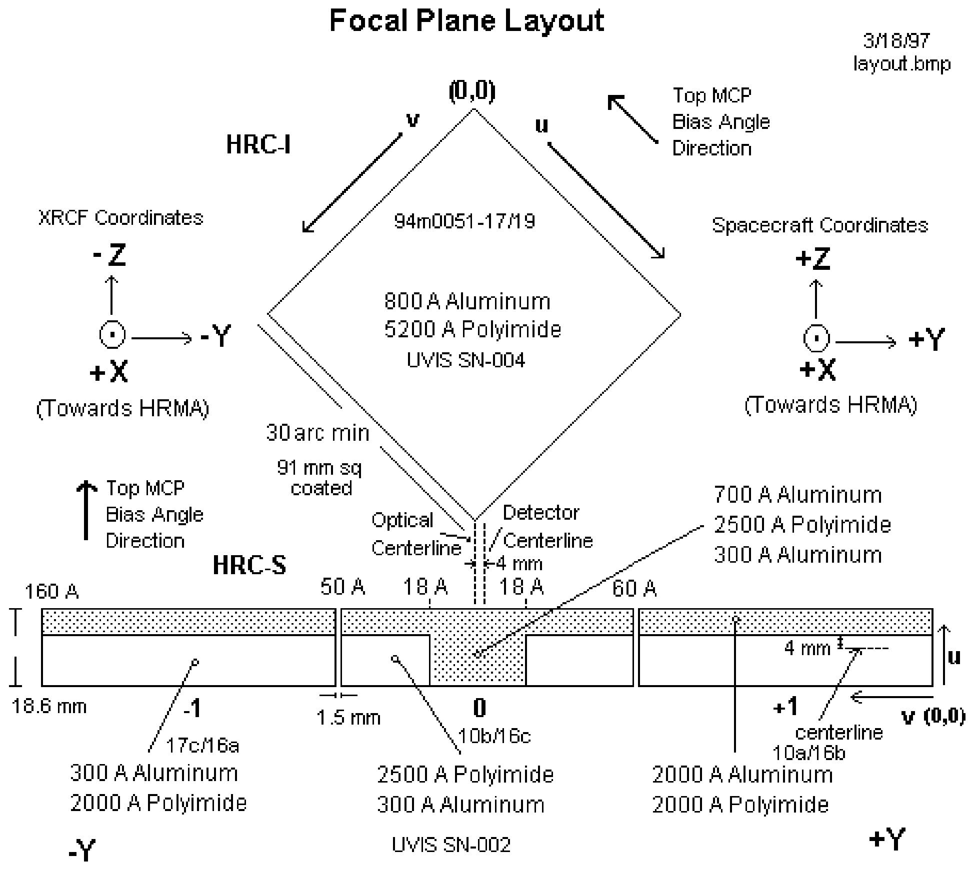

Figure 1: The material composition of the UVIS-I and UVIS-S are shown above. Where there is only a single side coated with aluminum, that side faces the High Resolution Mirror Assembly (HRMA) of AXAF. For the HRC-S Inner "T", it is the side with the 700Å coating that faces the HRMA. The figure also shows the relative orientation of the HRC-I and HRC-S in the instrument focal plane.

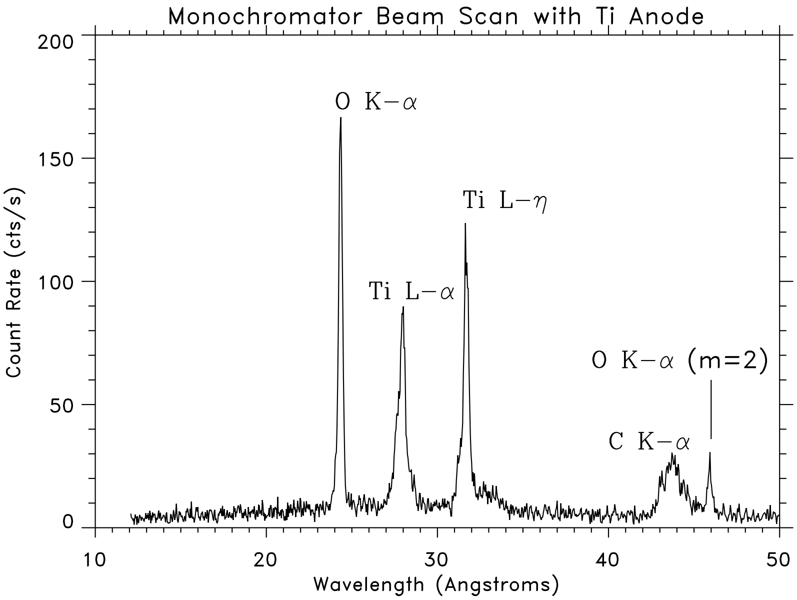

Figure 2: Example of a typical monochromator beam scan to identify the first order x-ray fluorescent lines associated with an anode. In this case, titanium. Note how the primary lines of interest, Ti L_α and L_η, dominate over the continuum.

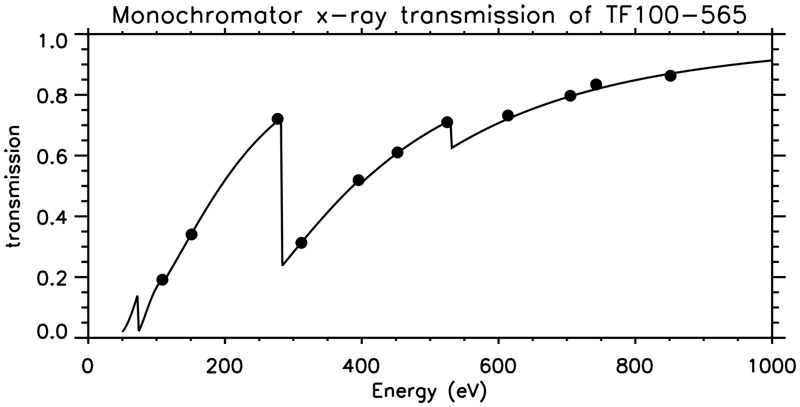

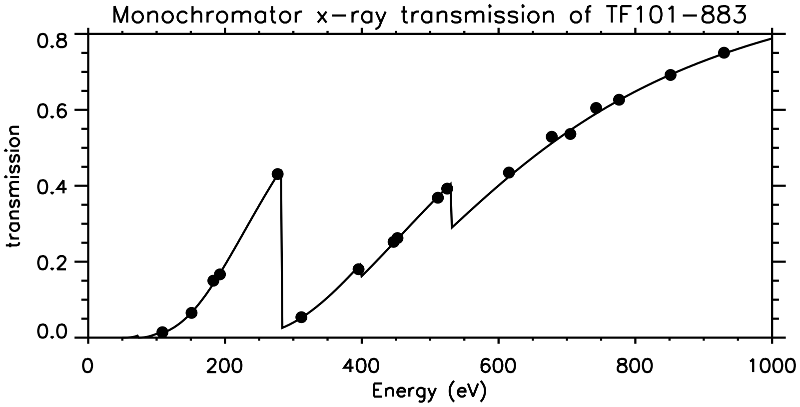

Figure 3: Modelled transmission curves for Luxel witness samples TF100-565 (top) and TF101-883 (bottom) based on the monochromator data. The transmission measurements taken with the SAO x-ray monochromator are plotted, also. The statistical error bars are smaller than the data points.

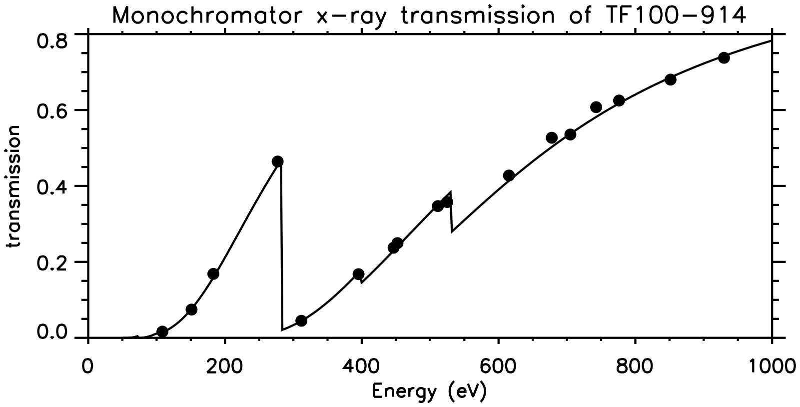

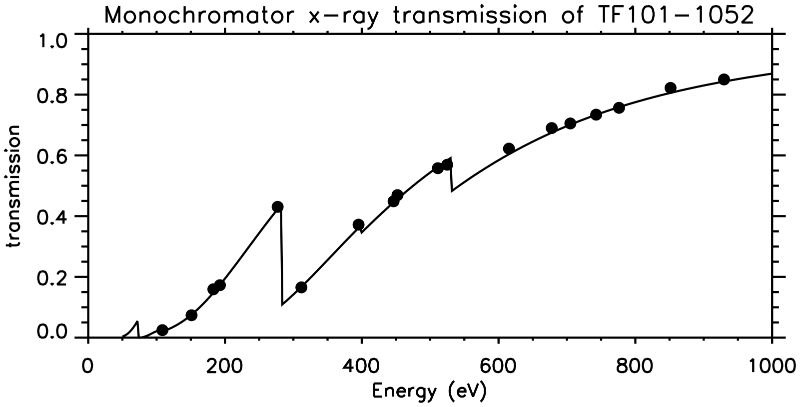

Figure 4: Modelled transmission curves for Luxel witness samples TF101-914 (top) and TF101-1052 (bottom) based on the monochromator data. The transmission measurements taken with the SAO x-ray monochromator are plotted, also. The statistical error bars are smaller than the data points.

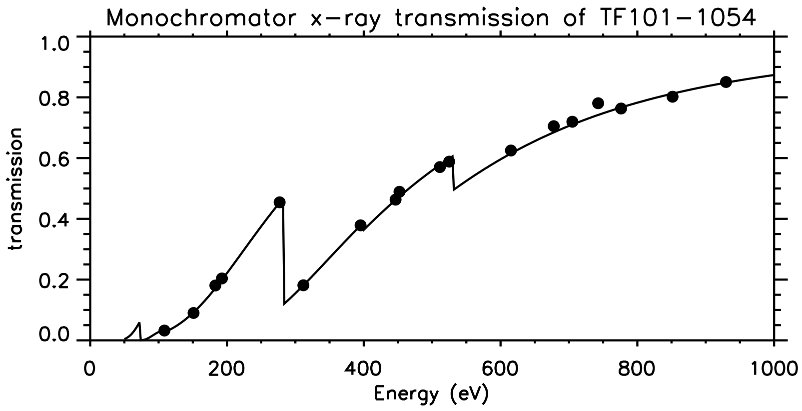

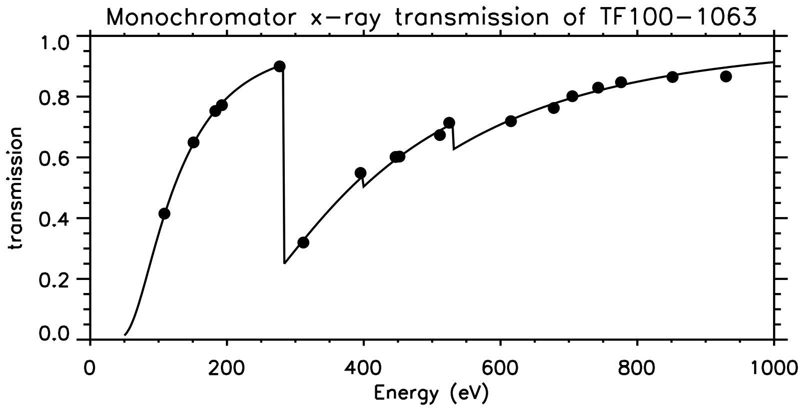

Figure 5: Modelled transmission curves for Luxel witness samples TF101-1054 (top) and TF100-1063 (bottom) based on the monochromator data. The transmission measurements taken with the SAO x-ray monochromator are plotted, also. The statistical error bars are smaller than the data points.

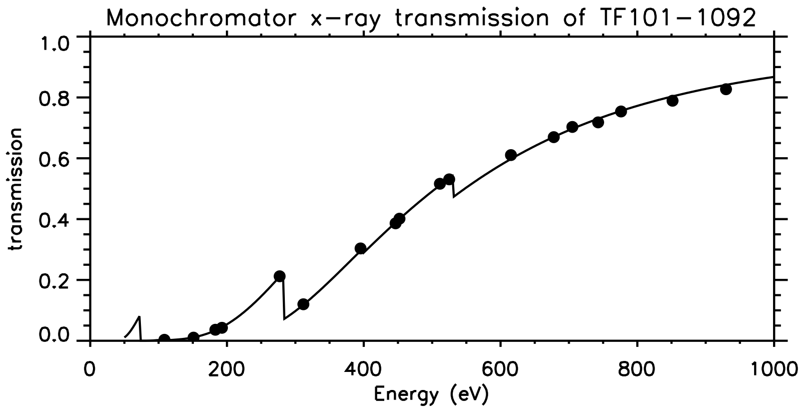

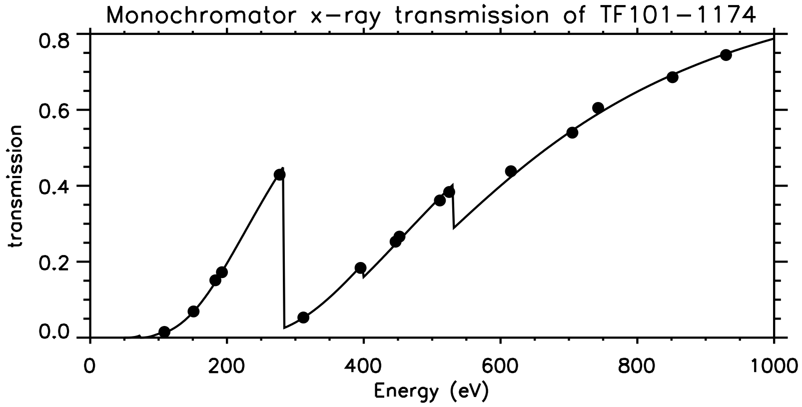

Figure 6: Modelled transmission curve for Luxel witness samples TF101-1092 (top) and TF101-1174 (bottom) based on the monochromator data. The transmission measurements taken with the SAO x-ray monochromator are plotted, also. The statistical error bars are smaller than the data points.

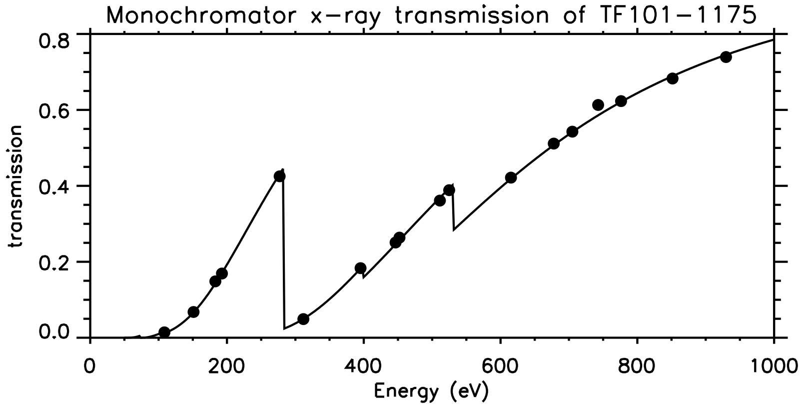

Figure 7: Modelled transmission curve for Luxel witness sample TF101-1175 based on the monochromator data. The transmission measurements taken with the SAO x-ray monochromator are plotted, also. The statistical error bars are smaller than the data points.

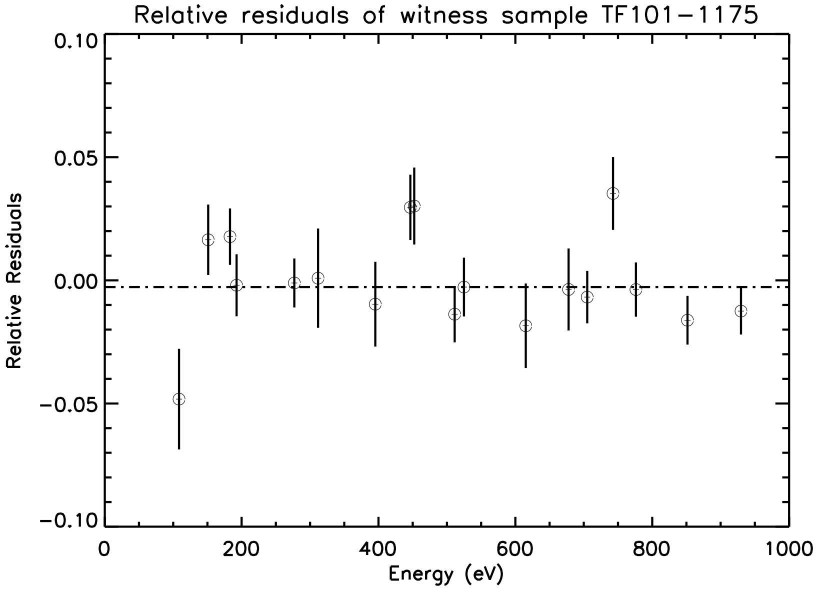

Figure 8: A plot of the relative residuals for witness sample TF101-1175, whose transmission was measured with the SAO x-ray monochromator. As discussed in the text, the fact that the median is close to zero indicates that there are no systematic errors.

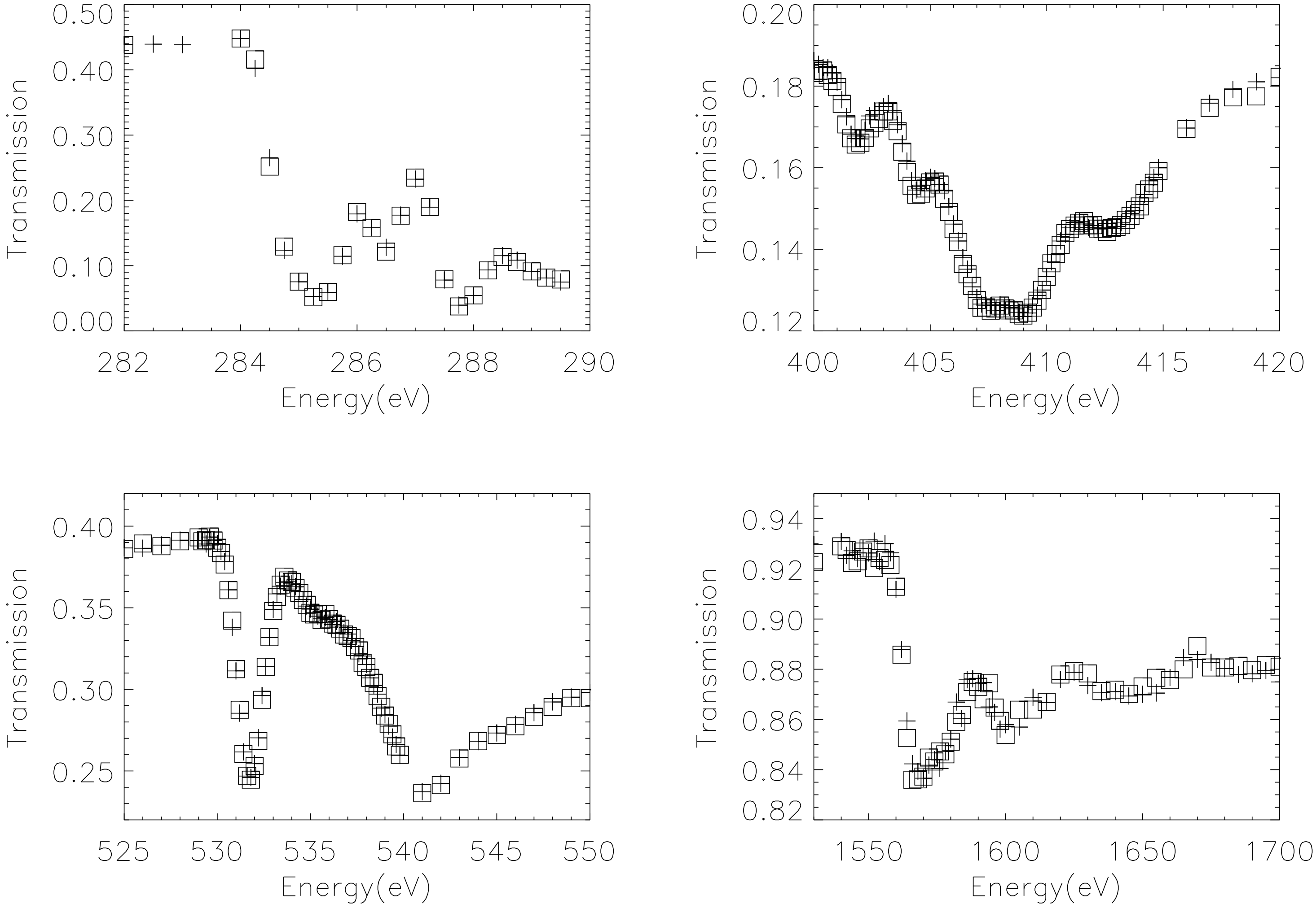

Figure 9: Absorption fine structures of the C, N, O, and Al K-edges measured in two different locations (plus symbol and square symbol) of witness sample TF101-1174.

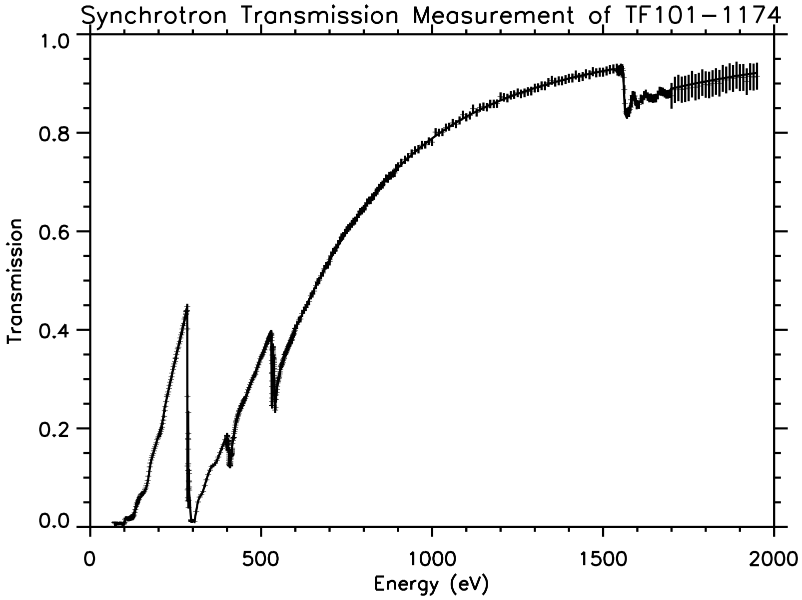

Figure 10: The measured transmission (the data points with error bars) for witness sample TF101-1174 at location 1. The best fit model, which incorporates the derived mass attenuation coefficients near the absorption edges, appears as the solid line.

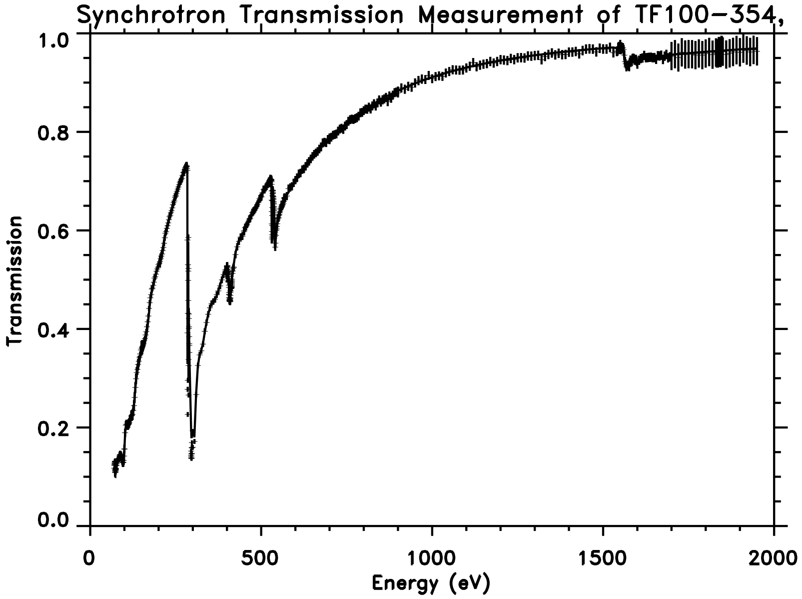

Figure 11: The measured transmission (the data points with error bars) for witness sample TF100-354. The best fit model, which incorporates the derived mass attenuation coefficients near the absorption edges, appears as the solid line.

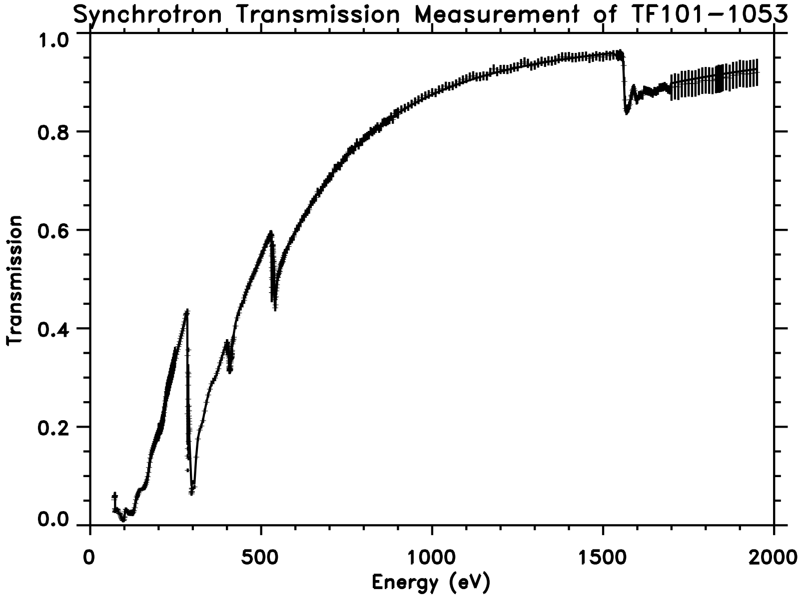

Figure 12: The measured transmission (the data points with error bars) for witness sample TF101-1053. The best fit model, which incorporates the derived mass attenuation coefficients near the absorption edges, appears as the solid line.

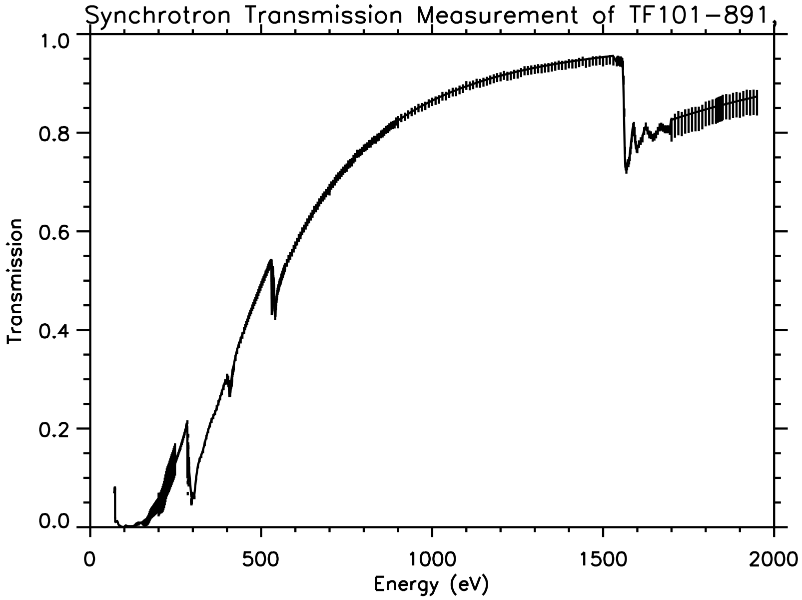

Figure 13: The measured transmission (the data points with error bars) for witness sample TF101-891. The best fit model, which incorporates the derived mass attenuation coefficients near the absorption edges, appears as the solid line.

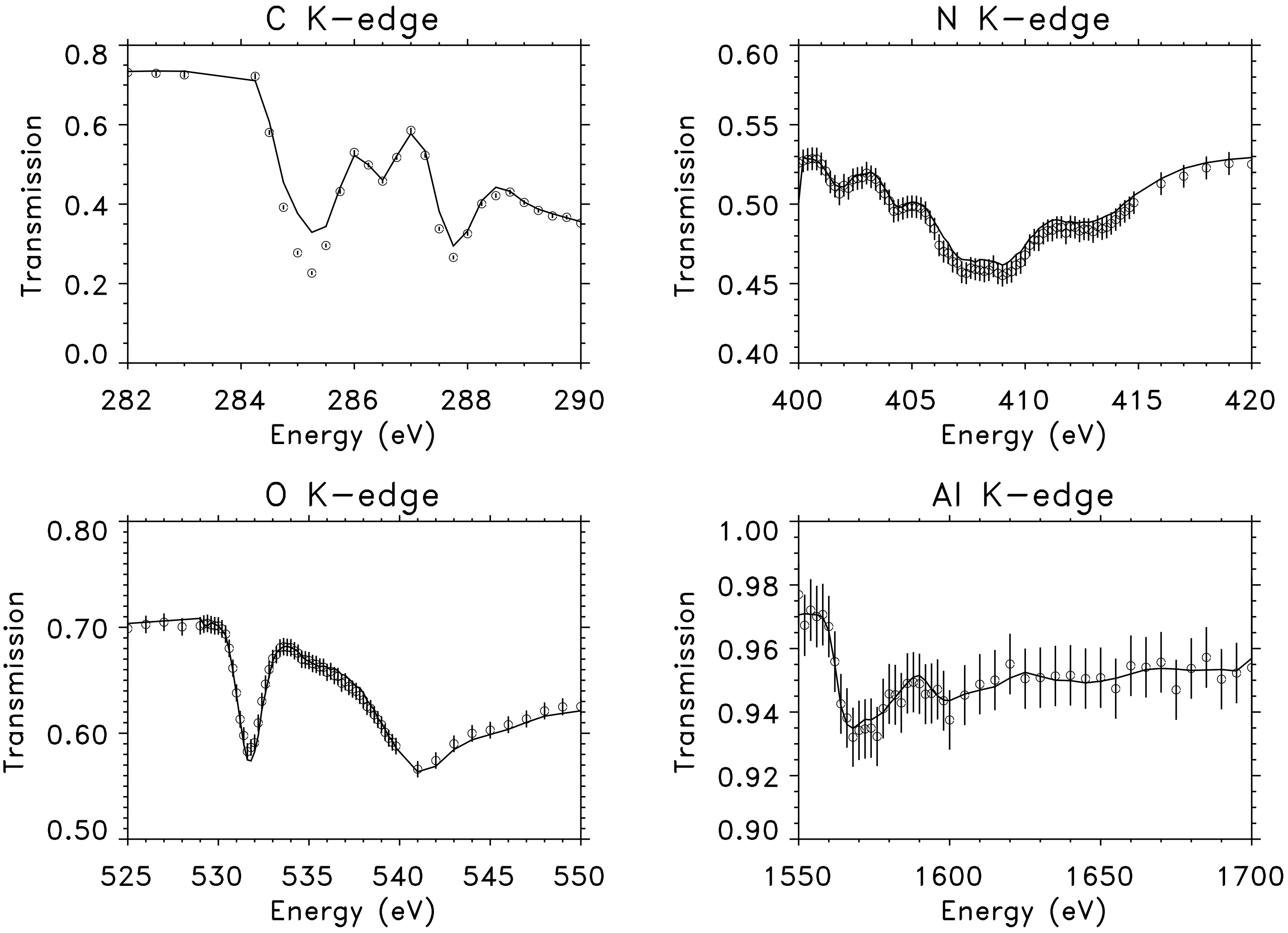

Figure 14: Each of the above plots gives a detailed look at how well the synchrotron transmission model (line plot) agrees with the synchrotron transmission measurements of filter TF100-354 at the absorption fine structure regions for the C, N, O and Al K-edges. Note that there are several energies in the C K-edge absorption region where the model and the data do not agree very well.

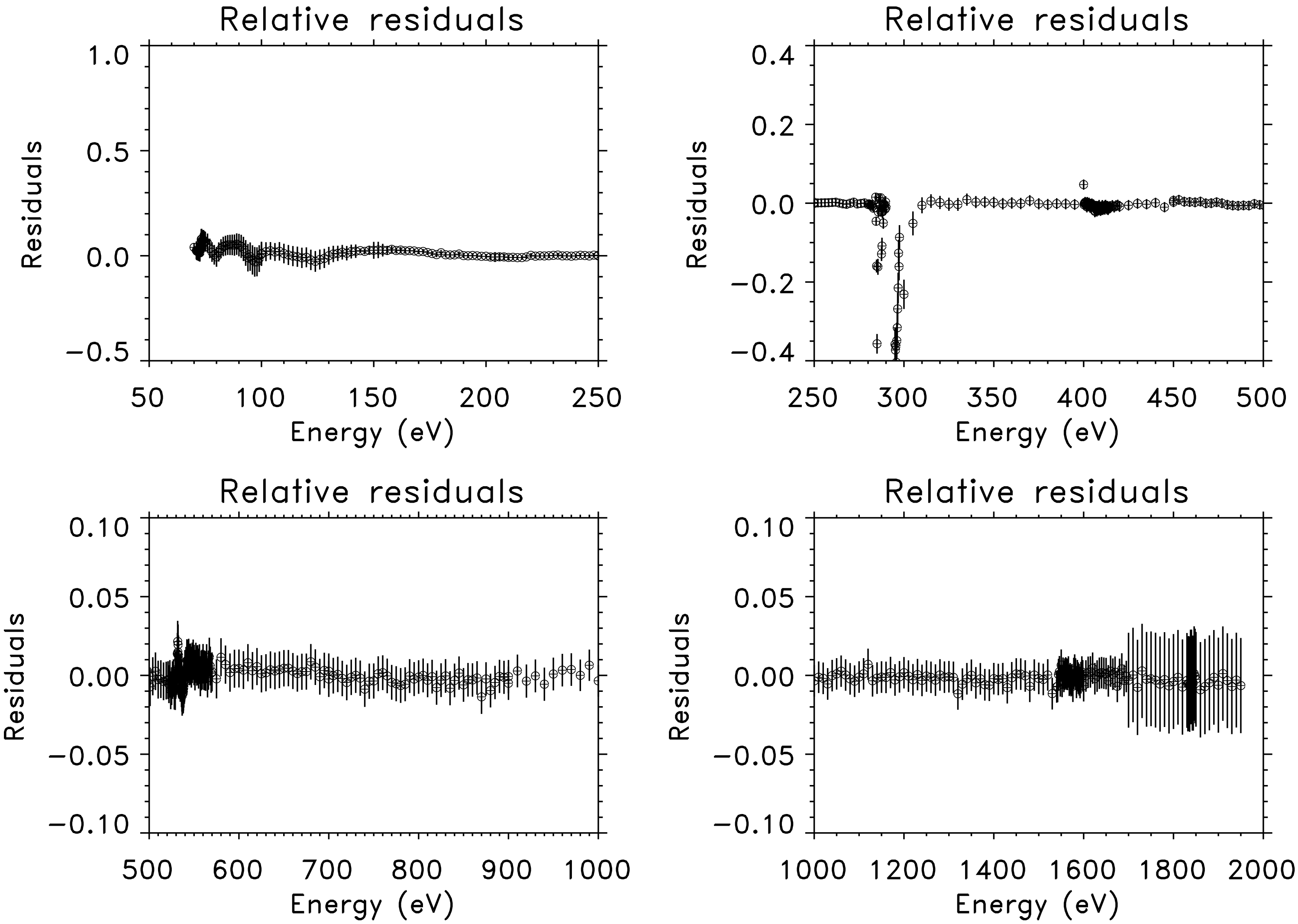

Figure 15: The relative residuals for synchrotron the transmission measurements and the model of filter TF100-354. Note that we obtain good agreement between the fit and the measurements, except at several energies near the carbon K-edge absorption region.

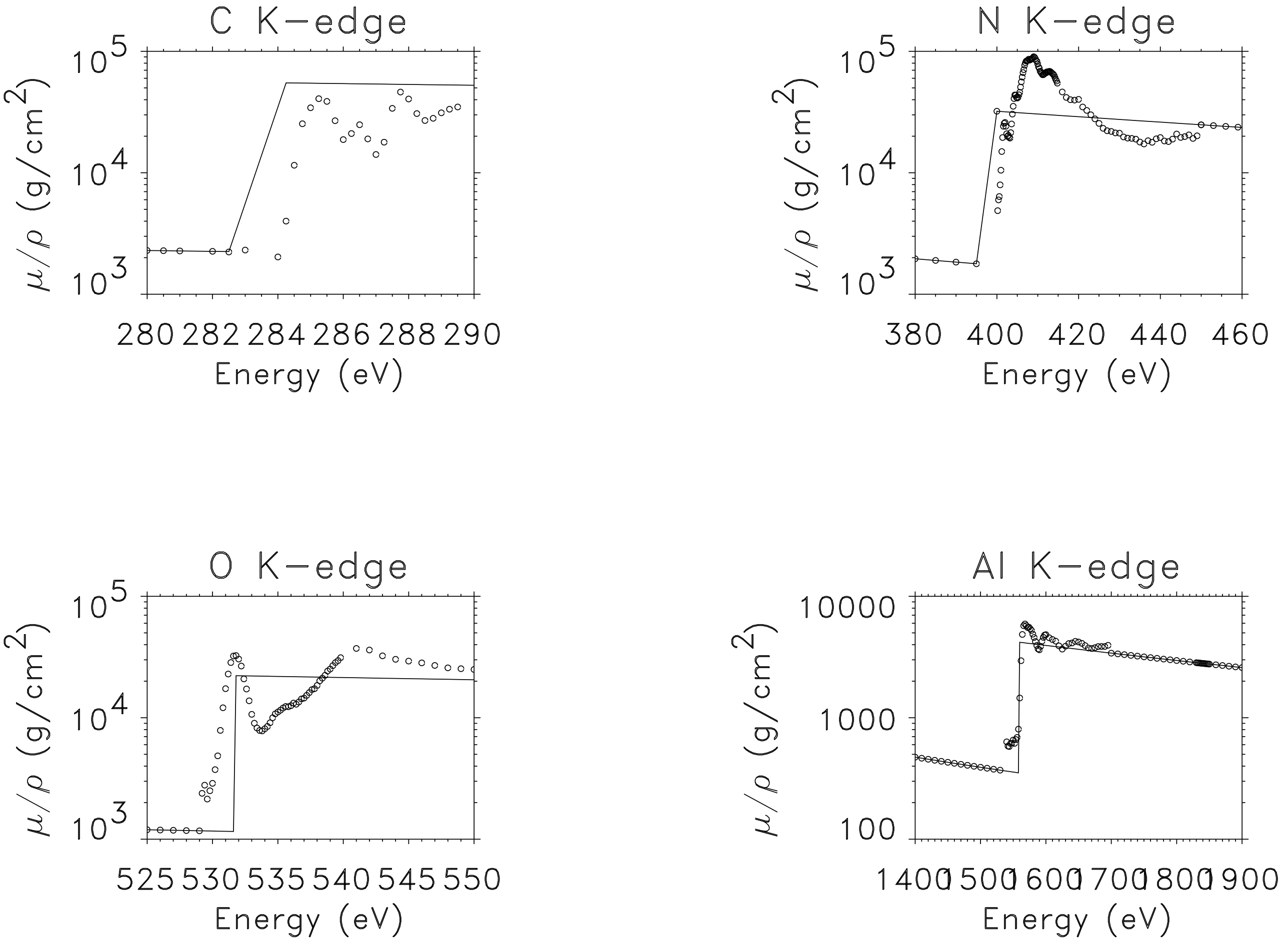

Figure 16: The above plots show the mass absorption coefficients of each element at its respective K-edge absorption region as developed from the transmission model based on the synchrotron measurements. The line plots in the graphs represent the 1982 Henke coefficients.

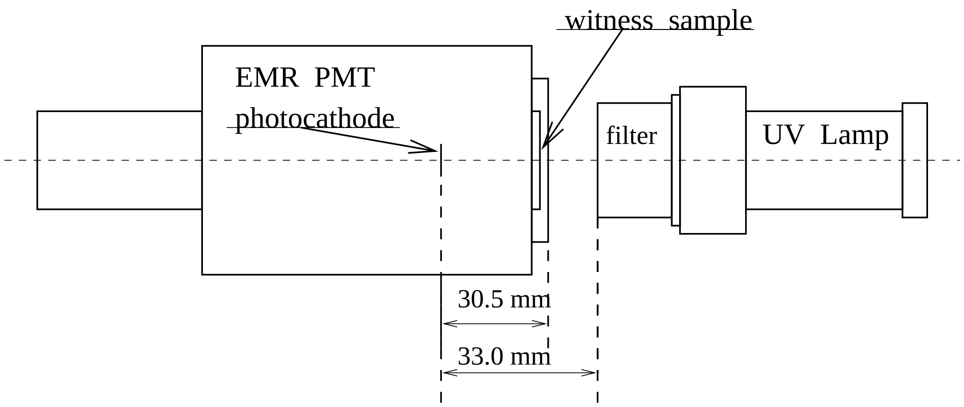

Figure 17: The setup used for witness sample UV flux measurements at 1470 Å and 2537 Å. To measure the flux from the UV light source, the PMT was replaced with a NIST UV photodiode.